Sign change of anomalous Hall effect and anomalous Nernst effect in the Weyl semimetal CeAlSi

Md Shahin Alam,[1,*] Amar Fakhredine,[2] Mujeeb Ahmad,[1] P. K. Tanwar,[1] Hung-Yu Yang,[3] Fazel Tafti,[3] Giuseppe Cuono,[1] Rajibul Islam,[1] Bahadur Singh,[4] Artem Lynnyk,[2] Carmine Autieri,[1,†] and Marcin Matusiak[1,5,‡]

[1]*International Research Centre MagTop, Institute of Physics, Polish Academy of Sciences, Aleja Lotników 32/46, PL-02668 Warsaw, Poland*
[2]*Institute of Physics, Polish Academy of Sciences, Aleja Lotników 32/46, PL-02668 Warsaw, Poland*
[3]*Department of Physics, Boston College, Chestnut Hill, Massachusetts 02467, USA*
[4]*Department of Condensed Matter Physics and Materials Science, Tata Institute of Fundamental Research, Mumbai 400005, India*
[5]*Institute of Low Temperature and Structure Research, Polish Academy of Sciences, ulica Okólna 2, 50-422 Wrocław, Poland*

(Received 17 October 2022; revised 14 December 2022; accepted 18 January 2023; published 3 February 2023; corrected 1 March 2023)

We report the anomalous Hall effect (AHE) and the anomalous Nernst effect (ANE) data for the noncollinear Weyl semimetal CeAlSi. The anomalous Hall conductivity (σ_{ij}^A) was measured for two different orientations of the magnetic field (B), namely σ_{yz}^A for $B||a$ and σ_{xy}^A for $B||c$, where a and c denote the crystallographic axes. We find that σ_{xy}^A and σ_{yz}^A are of opposite sign and both are large below the Curie temperature (T_C). In the paramagnetic phase, σ_{xy}^A rises even more and goes through a maximum at $T \approx 170$ K, whereas the absolute value of σ_{yz}^A decreases with increasing temperature. The origin of the sign difference between σ_{xy}^A and σ_{yz}^A was attributed to the reconstruction of the band structure under the variation of the spin orientation. Further, in a system where humps in the AHE are present and scalar spin chirality is zero, we show that the **k**-space topology plays an important role to determine the transport properties at both low and high temperatures. We also observed the anomalous contribution in the Nernst conductivity (α_{xy}^A) measured for $B||c$. α_{xy}^A/T turns out to be sizeable in the magnetic phase and above T_C slowly decreases with temperature. We were able to recreate the temperature dependencies of σ_{xy}^A and α_{xy}^A/T in the paramagnetic phase using a single band toy model assuming a nonzero Berry curvature in the vicinity of the Weyl node. A decisive factor appears to be a small energy distance between the Fermi level and a Weyl point.

DOI: 10.1103/PhysRevB.107.085102

I. INTRODUCTION

Topological Weyl semimetals (WSMs) are characterized by linear energy dispersions of the valence and conduction bands touching each other in momentum space at Weyl nodes [1–4]. The emergence of massless Weyl fermions as low-energy excitations manifests in many exotic physical effects like the presence of Fermi arcs on the surface [5], chiral anomaly induced negative magnetoresistance [6], chiral zero sound effect [7,8], etc. The subclass of WSMs that also exhibit magnetic ordering is a particularly interesting object of study [9–15]. These materials allow, for example, the manipulation of the anomalous Hall and anomalous Nernst effect [16,17], which is interesting from both scientific and applicative points of view. Recently, huge efforts have been made to investigate the sign change of the anomalous Hall effect (AHE) in Weyl fermions or closely relevant systems as the collinear ferromagnet $SrRuO_3$ [18]. It turns out that many factors, such as the value of the magnetization [19], the presence of the interface which can tune the spin-orbit coupling (SOC), or breaking of the inversion symmetry [20], can change the sign of AHE. Moreover, in the presence of the sign change, the anomalous Hall effect may take values smaller than other features, such as humps in the hysteresis loop of AHE [19,20]. The presence of these humps seems to be particularly favored by a large spin-orbit coupling as well as the absence of inversion symmetry [19,20] and in CeAlSi they were dubbed the loop Hall effect [21]. In CeAlSi, the humps are related to the **k**-space topology [21]. In order to get more insight into the **k**-space topology that governs these humps in CeAlSi, we investigated CeAlSi focusing on the transport properties in magnetic fields and looking for the sign change of the AHE. Additionally, we also measured the anomalous Nernst effect (ANE), whose response to nonzero Berry curvature around the Fermi energy is different than that expected for AHE. In the paramagnetic phase of CeAlSi, the simultaneous temperature evolution of both ANE and AHE can be well described by a simple model assuming the presence of the Weyl node about 20 meV from the Fermi level. The paper is organized as follows: We describe the material and methods in Sec. II; in Sec. III, we present our experimental results; in Sec. IV, we discuss our results, and in Sec. V we summarize our conclusions.

II. MATERIAL AND METHODS

CeAlSi single crystals were grown by a self-flux method using the Canfield crucible sets. The starting materials were weighed in the ratio Ce : Al : Si = 1 : 10 : 1, placed inside a crucible in an evacuated quartz tube, heated to 1000 °C at 3 °C/min, held at 1000 °C for 12 h, cooled to 700 °C at

*shahin@magtop.ifpan.edu.pl
†autieri@magtop.ifpan.edu.pl
‡matusiak@magtop.ifpan.edu.pl

0.1 °C/min, stayed at 700 °C for 12 h, and centrifuged to decant the residual Al flux.

For electrical and thermoelectrical transport measurements a suitable single crystal was cut into a plate with dimensions of $1.4 \times 1.3 \times 0.4$ mm^3 with sides parallel to the natural crystallographic $a \times a \times c$ axes. The electrical and thermal currents were applied along the longest side of the sample (a axis), while the magnetic field (B) was applied parallel to the c axis and perpendicular to the thermal and electrical currents. For electrical measurements with B applied along the crystallographic a axis we selected another single crystal, which was cut into a plate with dimensions of $0.2 \times 2.9 \times 0.6$ mm^3 ($a \times a \times c$). The electrical current (J) was applied along the a axis and B was perpendicular to the current and parallel to another a axis.

For the electrical measurements, the contacts were arranged in the Hall-bar geometry with 25-μm-thick gold wires attached to the sample using DuPont 4929N silver paste. During the measurements of thermoelectric power (S_{xx}) and Nernst signal (S_{yx}) the sample was mounted between two blocks made of phosphor bronze. The temperature difference was determined using two Cernox thermometers and the thermal gradient was implied using a strain gauge as a resistive heater. For selected temperatures, the magnetic field was swept from −14.5 to +14.5 T to extract the field voltage components that were antisymmetric and symmetric in B. All the presented data were symmetrized and antisymmetrized for the positive and negative magnetic fields.

Magnetic properties of the sample have been investigated using a Quantum Design Magnetic Property Measurement System MPMS XL equipped with a superconducting quantum interference device. The reciprocating sample option has been chosen to provide a precision of about 10^{-8} emu during the direct current (dc) measurements. A magnetic moment as a function of external dc magnetic field has been measured in the range –7 to +7 T after cooling at zero field. To study the temperature dependences of susceptibility, alternative current (ac) option has been utilized. An ac field of 1 Oe amplitude and 1 kHz of frequency has been applied during the measurements.

III. RESULTS

The electrical transport properties of CeAlSi were studied for two different orientations of the magnetic field (B), which was applied along the a axis (magnetically easy) or along the c axis (magnetically hard). The temperature (T) dependence of the longitudinal resistivity (ρ_{xx}) for the electrical current (J) parallel to the a axis and $B = 0$ T (see Fig. 1) shows semimetallic behavior with the residual resistivity ratio of 3.2 (see Fig. 1). A kink at $T_C \approx 8.5$ K appears due to the transition from the high-temperature-paramagnetic (PM) phase to the low-temperature ferromagnetic (FM) phase [21]. The value of the transition temperature and overall temperature dependence of ρ_{xx} agree well with the previous reports [21–23]. The magnetic field dependencies of the longitudinal resistivity (ρ_{xx}) and Hall resistivity (ρ_{yx}) ($B||c$ and $J||a$), as well as ρ_{yy} and ρ_{zy} (B and $J||a$, $B\perp J$) are shown in Fig. 2. The Hall resistivities for both orientations of B [Figs. 2(b) and 2(d)] becomes negative at low temperature and high magnetic field,

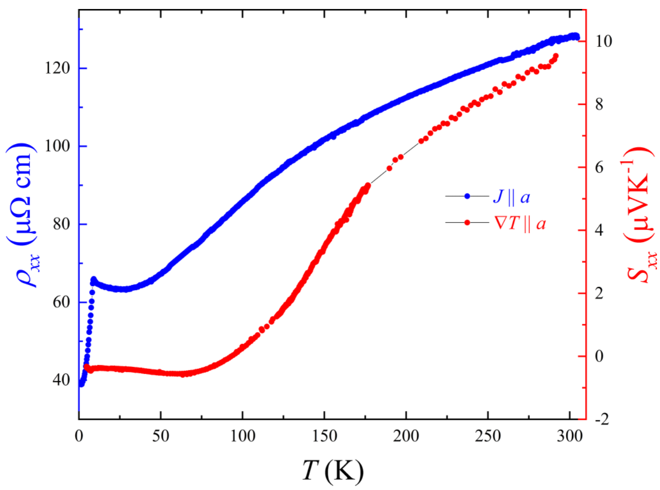

FIG. 1. Temperature dependencies of the zero field resistivity (ρ_{xx}) and the thermoelectric power (S_{xx}) of the noncollinear Weyl semimetal CeAlSi with the current (J) or thermal gradient (∇T) applied parallel to a axis.

which indicates that the electronlike charge carriers dominate electrical transport in this region. Specifically, at $B = 14.5$ T, $\rho_{yx} \approx -35$ $\mu\Omega$ cm for $T \approx 5.4$ K and $\rho_{zy} \approx -65$ $\mu\Omega$ cm for $T \approx 1.7$ K. However, the high-field slope of the ρ_{yx} Hall resistivity evolves with temperature and becomes slightly positive at room temperature ($d\rho_{yx}/dB = 1.2 \times 10^{-9}$ m^{-3} C^{-1} at $T = 301$ K), which might be due to the slowly increasing with temperature role of holes in the electrical transport.

A prominent characteristic of the Hall resistivity in CeAlSi is its nonlinear field dependence [see Fig. 2(b)]. Although this type of behavior might be due to simultaneous contributions from different types of charge carriers [24,25], it seems to be not the case in CeAlSi. In fact, ρ_{yx} varies linearly at high field, but $\rho_{yx}(B)$ does not extrapolate to $\rho_{yx} = 0$ $\mu\Omega$ cm at $B = 0$ T. The field dependence of ρ_{yx} cannot be satisfactorily explained within the two-band model approach as shown in Fig. S1 in the Supplemental Materials (SM) [26] (see also Refs. [27–31] therein), which is in line with the previous reports indicating that the transport in CeAlSi is dominated at low temperatures by a single type of charge carrier [32]. A likely cause for the nonlinear behavior of the Hall resistivity in CeAlSi is a contribution from the anomalous Hall effect (AHE) [21,33–36]. In general, the magnetic field dependencies of Hall resistivity in the presence of the anomalous contribution can be expressed as

$$\rho_{yx} = R_0 B + \rho^A_{yx}, \tag{1}$$

where R_0 is the ordinary Hall coefficient and ρ^A_{yx} is the anomalous Hall resistivity. To determine R_0 and to separate ρ^A_{yx} (or ρ^A_{zy}) from the total Hall resistivity, $\rho_{yx}(B)$ [or $\rho_{zy}(B)$] was fitted with a linear function in the high-field regime (>3 T) [see Figs. 3(a) and 3(b)]. At low temperature, the fitting range of the former was restricted to $B_{\max} = 9$ T, because of a change in the $\rho_{yx}(B)$ slope happening at this field. This anomaly is also visible in the field dependencies of ρ_{xx} [Fig. 2(a)] and it is likely related to the magnetic phase transition caused by increasing magnetic field perpendicular to the initially FM

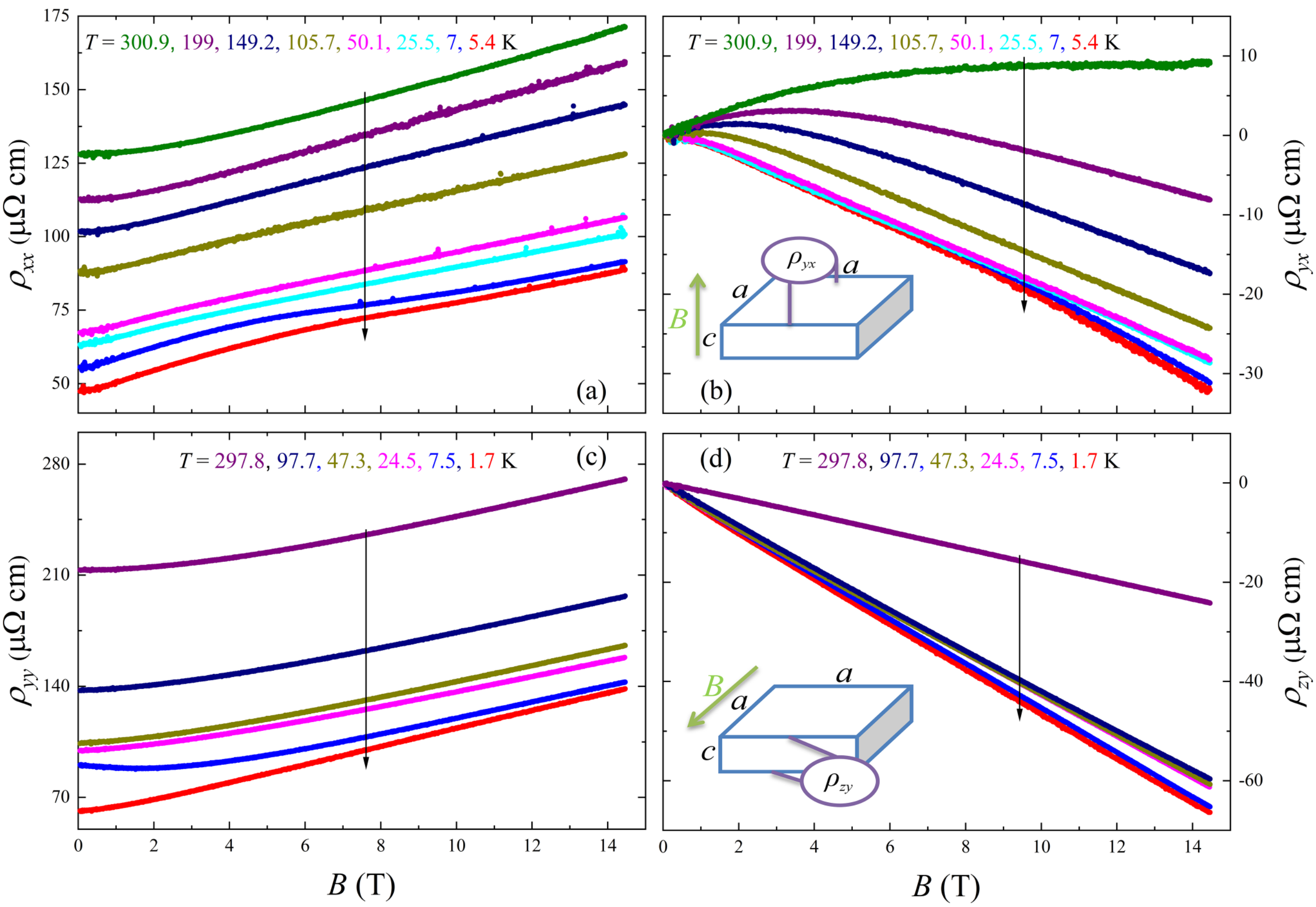

FIG. 2. Magnetic field dependencies of the longitudinal resistivity and Hall resistivity in CeAlSi for two different configurations of the sample. For $J \parallel a$ and $B \parallel c$, (a) longitudinal resistivity (ρ_{xx}); (b) Hall resistivity (ρ_{yx}), $J \parallel a$, $B \parallel a$, and $B \perp J$; (c) longitudinal resistivity (ρ_{yy}); (d) Hall resistivity (ρ_{zy}). The black vertical arrows in all the panels indicate variation of the temperature.

ordered spins [37]. The extracted field dependencies of the anomalous Hall resistivity for $B||c$ (ρ^A_{yx}) and $B||a$ (ρ^A_{zy}) are presented in Figs. 3(c) and 3(d). In the FM phase, both ρ^A_{yx} and ρ^A_{zy} are sizeable, but different in sign and magnitude. In the PM phase, the absolute value of ρ^A_{yx} becomes significantly larger than ρ^A_{zy}.

In general, the AHE can be of intrinsic or extrinsic origin and the latter can be due to the skew-scattering or side-jump processes [27]. If there were a contribution from an extrinsic mechanism, one would expect a specific relation between the resulting anomalous Hall conductivity (AHC, σ^A_{ij}) and the longitudinal conductivity (σ_{ii}). Namely, for the skew scattering, the AHC should follow a linear relationship with the longitudinal conductivity, whereas for the side jump (which is expected to be somewhat smaller [38]) $\sigma^A_{ij} \sim \sigma^2_{ii}$ [39]. In our data we observe neither of them (Fig. S2 in the SM [26]). Furthermore, in topological semimetals with the Fermi level in the vicinity of Weyl nodes, the AHE has been predicted to be predominantly intrinsic and determined by the location of the Weyl points [40,41]. Since CeAlSi has been identified as a Weyl semimetal with Weyl nodes close to the Fermi level [21], one can expect a nonzero AHE due to its nontrivial topological properties [21–23,42]. These are expected to manifest themselves also in other transport phenomena.

The magnetic field dependence of thermoelectric power with the thermal gradient $\nabla T||a$ and $B||c$ is presented in Fig. 4(a). $S_{xx}(B)$ can be satisfactorily fitted with the semiclassical phenomenological model proposed by Liang *et al.* [43]:

$$S_{xx}(B) = S^0_{xx}\,\frac{1}{1+(\mu B)^2} + S^\infty_{xx}\,\frac{(\mu B)^2}{1+(\mu B)^2}, \qquad (2)$$

where S^0_{xx} and S^∞_{xx} are the amplitudes of the thermopower at zero and high field limits respectively, and μ is the mobility of charge carriers. A shift of S^0_{xx} from negative at low temperatures to positive at high temperatures can be a sign of an increase in the participation of holes, which is consistent with the Hall resistivity data discussed earlier. If these holes have low mobility, then their contribution will be only slightly field dependent and will not disturb the fitting procedure, which in fact works well for all the data [see Fig. 4(a)]. At low temperatures, we restricted again the fitting field range due to the change in $S_{xx}(B)$ slope at $B \sim$ 8–9 T owing to the aforementioned field-induced transition. The temperature dependence of S_{xx} at zero magnetic field is shown in Fig. 1.

Figure 4 presents the field dependencies of the Nernst effect signal measured for a configuration analogous to ρ_{yx}, i.e., $\nabla T \parallel a$ and $B||c$. Results are fitted with the empirical model [44] describing the behavior of the Nernst effect in a

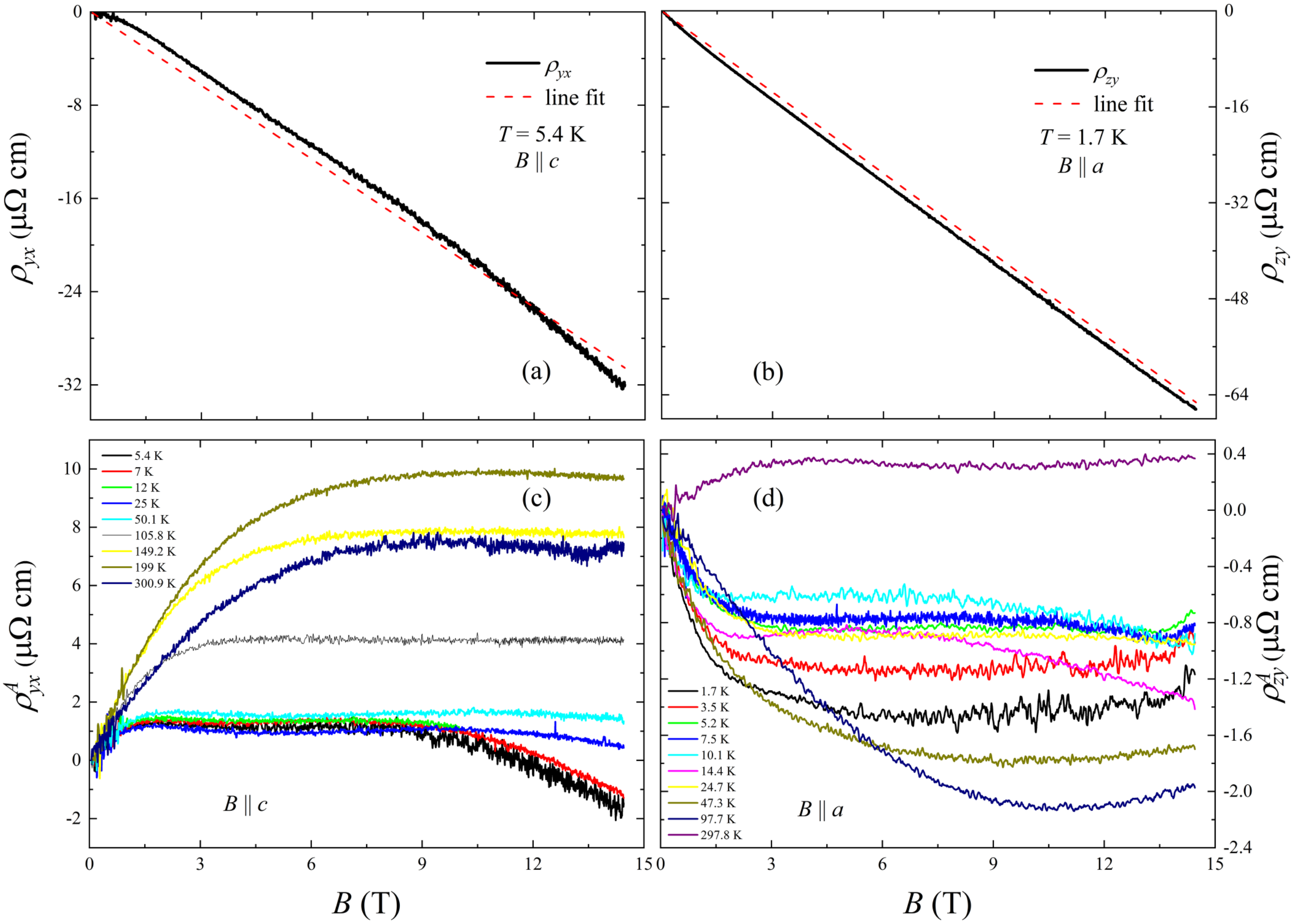

FIG. 3. Magnetic field dependencies of the Hall resistivity in CeAlSi: (a) Hall resistivity (ρ_{yx}) as a function of B at $T = 5.4$ K (black line); (b) Hall resistivity (ρ_{zy}) as a function of B at $T = 1.7$ K (black line). Red dashes lines in (a) and (b) represent the high-field ($B > 3$ T) linear fits. (c) Anomalous contribution to the Hall resistivity (ρ^A_{yx}) extracted from $\rho_{yx}(B)$ for several temperatures. (d) Anomalous contribution to the Hall resistivity (ρ^A_{zy}) extracted from $\rho_{zy}(B)$ for several temperatures.

topologically nontrivial material. Here, the total Nernst signal is similar to the Hall resistivity and is divided into a normal (S^N_{yx}) and an anomalous (S^A_{yx}) part:

$$S_{yx} = S^N_{yx} + S^A_{yx}, \tag{3}$$

where their field dependencies are expressed as

$$S^N_{yx} = S^N_0 \frac{\mu}{1 + (\mu B)^2}, \tag{4}$$

$$S^A_{yx} = S^A_{yx} \tanh{(B/B_s)}, \tag{5}$$

μ is the mobility, and B_s is the saturation field at which the plateau of the anomalous signal is reached. Apparently, the field dependencies of S_{yx} cannot be described only by the conventional Nernst contributions [Eq. (4)] (see Fig. S1 in the SM [26]), but they are very well approximated when the anomalous component [Eq. (5)] is taken into consideration [see Fig. 4(b)]. The temperature dependence of the normalized (divided by temperature) S^A_{yx} is displayed in the inset of Fig. 5(b). In the FM phase S^A_{yx}/T steeply increases with decreasing the temperature (reaching $S^A_{yx} \approx -0.1$ μVK^{-2} at 2.5 K), but also in the PM phase there is a nonvanishing anomalous contribution (in the order of $S^A_{yx} \approx -0.02$ μVK^{-2}) slowly decreasing with temperature.

IV. DISCUSSION

The anomalous Hall (σ^A_{ij}) and transverse thermoelectric (α^A_{ij}) conductivities can be calculated as [45–47]

$$\sigma^A_{ij} = \frac{\rho^A_{ji}}{\rho^2_{ii}}, \tag{6}$$

$$\alpha^A_{ij} = S^A_{ji}\sigma_{ii} - S_{ii}\sigma^A_{ij}, \tag{7}$$

if $\rho_{ii} \gg \rho^A_{ji}$. The resulting temperature dependences of $\sigma^A_{xy}(T)$ and $\alpha^A_{xy}/T(T)$ are presented in Fig. 5. Two temperature regions can be distinguished: (i) $T < T_C$ (FM phase) and (ii) $T > T_C$ (PM phase).

(i) In the ferromagnetic phase σ^A_{xy} gradually increases with decreasing temperature reaching ~550 Ω^{-1} cm^{-1} at $T = 5.4$ K [Fig. 5(a)]. The loop Hall effect (LHE) was reported to occur in CeAlSi in the FM phase with $B||c$ field orientation [21], but the appearance of this phenomenon changes from sample to sample depending on a slight off-stoichiometry

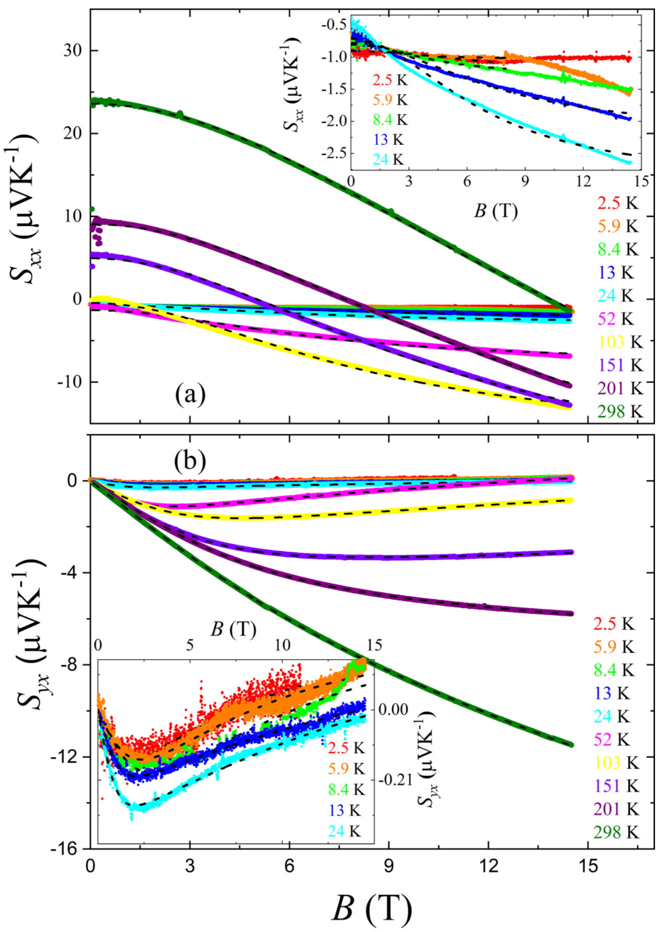

FIG. 4. Magnetic field dependence of the Seebeck (a) and Nernst (b) signal in CeAlSi for various temperatures. Insets show low-temperature field dependencies of the respective coefficients. The black dashed lines in (a) and (b) show fits prepared using Eqs. (2) and (4).

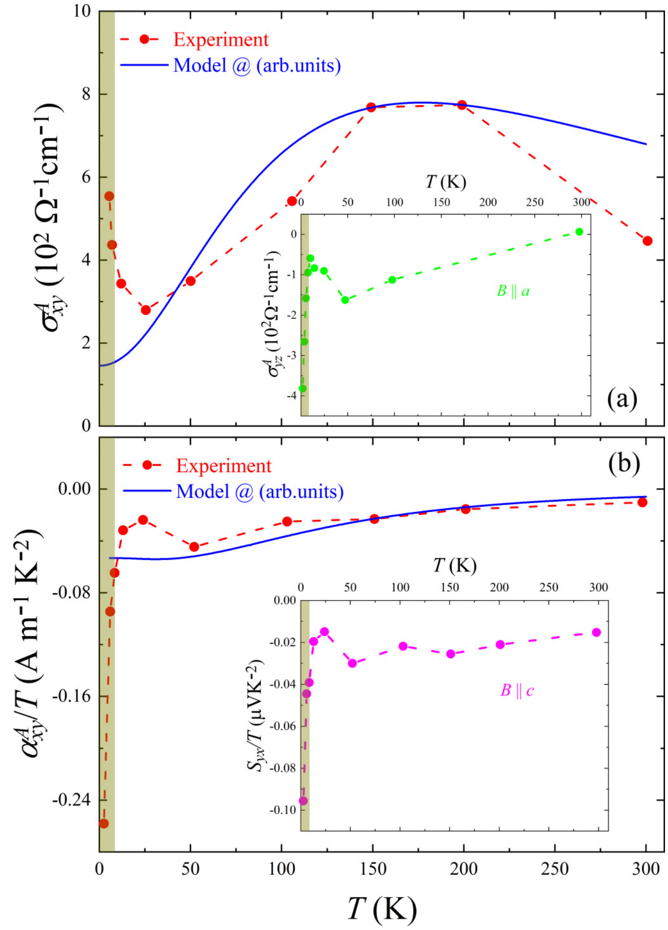

FIG. 5. The temperature dependencies of the anomalous Hall conductivity (σ^A_{xy}) (a) and the anomalous Nernst conductivity (b) for $B||c$ in CeAlSi. Inset in the upper panel shows temperature dependent anomalous conductivity (σ^A_{yz}) for $B||a$; inset in the lower panel presents the temperature dependence of normalized anomalous Nernst effect for $B||c$. Blue solid lines in both panels present the σ^A_{xy} and α^A_{xy}/T T emperature dependencies calculated in arbitrary units using Eqs. (8) and (9). Vertical dark yellow areas in all panels represent the FM regime.

of Si and Al [21]. In this material class, the Weyl nodes are generated due to the lack of inversion symmetry in the noncollinear phase [21,22], while for the ferromagnetic phase Weyl points can be generated also by the breaking of time-reversal symmetry [42]. A recent study on CeAlSi suggested a nontrivial π Berry phase that has been experimentally reported in the FM regime for the magnetic field oriented along the c axis [23].

Similarly to σ^A_{xy}, we also determined the T dependence of σ^A_{yz} for the magnetic field oriented along the easy axis. $\sigma^A_{yz}(T)$ is presented in the inset of Fig. 5(a). We found $\sigma^A_{yz} \approx -380\ \Omega^{-1}\ \mathrm{cm}^{-1}$ at $T = 1.7$ K, a magnitude that is consistent with the previous reports [21]. Differences in values of σ^A_{xy} and σ^A_{yz} can be attributed to the anisotropic electronic structure of CeAlSi, while the observed sign change may be relevant for the detection of topological features in the AHE. Its occurrence, for example, was recently associated with the presence of humplike features in $\rho_{yx}(B)$ [19,48]. A physical origin of this anomaly is under strong debate, but it could derive from topological effects in the k space and/or in the real space. In CeAlSi the appearance of the analogous loop Hall effect appears to be dependent on the position of the Fermi level [21].

We study the magnetic configurations with spins along the a and the c axis (x and z, respectively) in addition to the noncollinear magnetic configuration that is the ground state. Using density functional theory (DFT) and Wannierization techniques, we perform the self-consistent and band structure calculations for different magnetic configurations to investigate the sign change of the AHE in the magnetic phase below $T_C = 8.5$ K.

From the self-consistent calculation, we note that the magnetization is mostly coming from the $4f$ electrons of Ce. The local magnetic moment per Ce atom is approximatively constant in all magnetic configurations. The magnetic moment for the $4f$ orbitals is 0.85–0.89μ_B where the lowest value is for the noncollinear magnetic configuration and the highest is for both collinear configurations. We have an intrinsic magnetic moment from $4f$ orbitals and an induced magnetic moment on the $5d$ orbitals of Ce that is $0.03\mu_B$ within DFT. The f electrons induce a ferromagnetic moment on

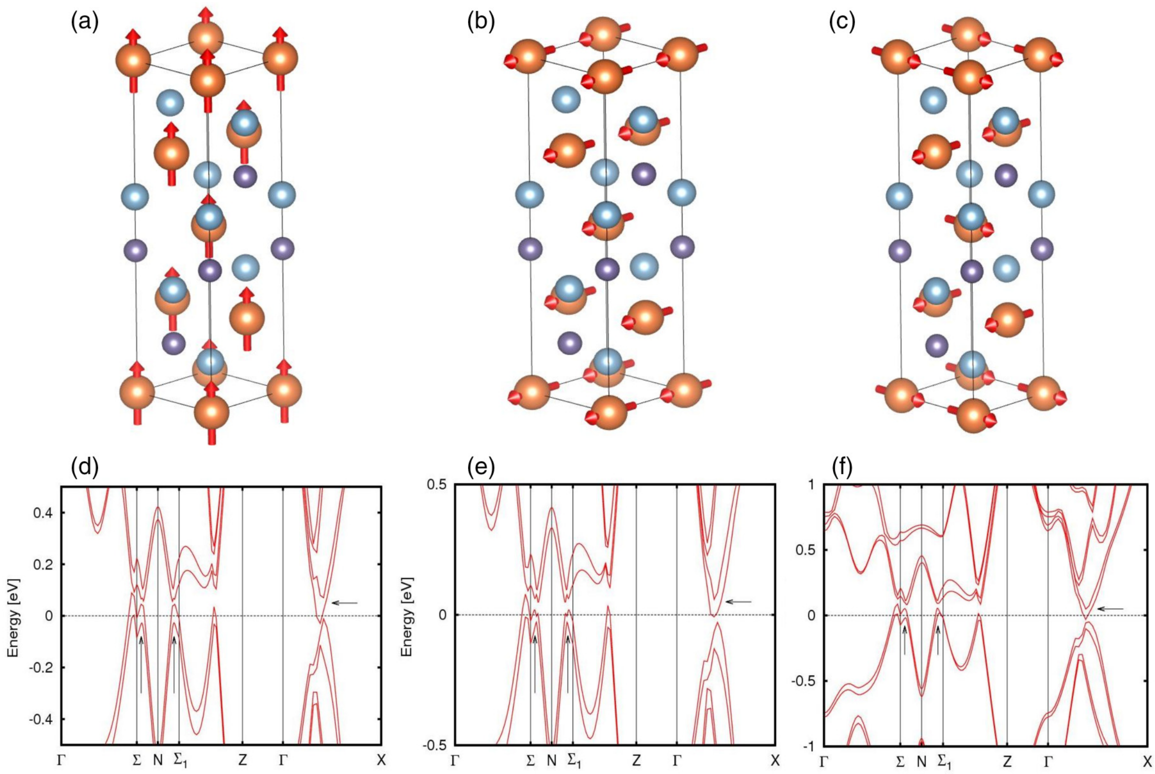

FIG. 6. Magnetic configurations and associated band structures of the CeAlSi Weyl semimetal. (a) Collinear FM order with spins aligned along the *a* axis. (b) Collinear FM order with spins aligned along the *c* axis. (c) Noncollinear FM order. (d)–(f) represent the band structure of CeAlSi along the high symmetry paths including spin-orbit coupling in the three mentioned configurations respectively. The vertical arrows represent the band crossings at the Fermi surfaces between **Σ**-**N** and N-$\mathbf{\Sigma_i}$, while the horizontal arrows point at the minimum of the conduction band between **Γ** and **X**.

the *d* electrons of Ce in the same fashion as happens in the $EuTiO_3/SrTiO_3$ system [49]. The presence of magnetic *f* electrons far from the Fermi level and *d* electrons at the Fermi level makes it difficult to produce a simplified tight-binding model containing both *d* and *f* orbitals. The bands associated with the Weyl points mainly come from the *d* electrons of Ce and the *sp* electrons of Al and Si as clearly visible in the local density of states (see part E in the SM [26]).

We report in Figs. 6(a)–6(c) the magnetic configurations with the Ce spins along the *a* axis, the *c* axis, and with the noncollinear configuration, respectively, where *a* and *c* are the lattice constants of the conventional unit cell shown in the figure. The band structures associated with these magnetic configurations are in the respective bottom panels in Figs. 6(d)–6(f). The main features of the three band structures are the same, but the different magnetic configurations slightly move the details of the low energy features and switch the position of the Weyl points [50]. One relevant change for the AHE appears along the high-symmetry path **Σ**-**N** and N-$\mathbf{\Sigma_i}$ where we can see at the position of the vertical arrows that the bands close to the Fermi level are slightly lower in energy in the case of the magnetic configuration with spin along the *c* axis shown in Fig. 6(e); as a consequence the minimum of the conduction band along **ΓX** goes higher in energy in Fig. 6(e). Therefore, the AHE will be modified by an energy shift approximatively equal to the difference between the Weyl points for the case with spin along the *c* axis ($E^{z}_{\rm WP}$) and the *a* axis ($E^{x}_{\rm WP}$). Defined as $\Delta E_{\rm WP} = E^{z}_{\rm WP} - E^{x}_{\rm WP} > 0$, this shift will be reflected in the AHE calculations. Basically, the different magnetic orderings influence the position of the Fermi level and the energy position of the Weyl points, and the anticrossing points close to the Fermi level.

It is known that close to the high-symmetry line **ΓX** T here are several Weyl points [42]. In CeAlSi, there are Weyl points from the breaking of the inversion symmetry and Weyl points from the breaking of the time-reversal symmetry. The Weyl points from the breaking of the time reversal present along **ΓX** are expected to be more sensitive to the orientation of the magnetic order, therefore strong changes in the AHE are expected.

Given the three band structures in Figs. 6(d)–6(f), we extracted the Wannier tight-binding model (see the SM for details [26]) and calculated the anomalous Hall effect for the three magnetic configurations shown in Fig. 7. We report σ_{xy} for the magnetic configuration with spin along the *c* axis (hard axis), and σ_{yz} for the configurations with spins along the *a* axis (easy axis) and the noncollinear phase. In the calculated energy range between −0.5 and 0.5 eV, the calculated AHC is always positive except for a negative spike present for all configurations. While for in-plane magnetic configuration this spike is at the Fermi level, for the out-of-plane magnetic configuration this negative spike is shifted by the quantity $\Delta E_{\rm WP}$ deriving from the band structure effects. This implies that the change of the magnetization from the *a* to the *c* axis plays a

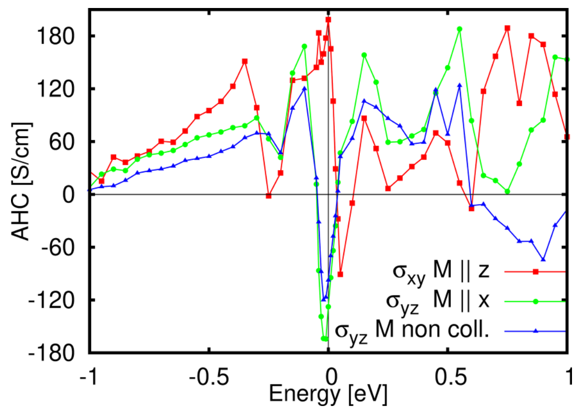

FIG. 7. Calculated intrinsic anomalous Hall conductivity for the collinear ferromagnetic configuration with spins along the *a* axis (green with circle points), along the *c* axis (red with square points), and in the noncollinear magnetic configuration (blue with triangle points). The energy range is between −1 and +1 eV. The Fermi level is set to zero for all three magnetic configurations.

role in inverting the sign of the anomalous Hall conductivity. The AHC is positive for the out-of-plane magnetic field and negative for the in-plane magnetic field in agreement with the experimental results reported in Fig. 5(a). The presence of consecutive and negative large values of the Berry curvature is a signature of the Weyl points; indeed, in a simplified Weyl points model, the Berry curvature goes from being strongly positive to strongly negative when you go from below to above the Weyl points [51] (see part D of the SM [26]). Hence, the sign change of AHE comes directly from the presence of the **k**-space topology (Weyl points) close to the Fermi level.

Our theoretical results developed at low temperatures could be qualitatively valid also above T_C, where the magnetization rotates from the easy axis towards the axis of the applied strong magnetic field. Since the Weyl points at the Fermi level do not come from $4f$-electron bands, we expect that AHE is weakly dependent if the induced magnetic moment on $5d$ electrons comes from the $4f$-Ce intrinsic magnetic moment or from the external magnetic field. Therefore, the AHE above Curie temperature can be large too and AHE below and above T_C can be of the same order of magnitude. Therefore, the large AHE in the paramagnetic phase emerges due to the presence of the **k**-space topology (Weyl points) close to the Fermi level. Indeed, the Weyl points are close to the Fermi level giving a large contribution even in the presence of the external magnetic field.

(ii) In the paramagnetic phase, the anomalous Hall conductivity for $B||a$ (σ_{yz}^A) decreases with increasing temperature and practically vanishes at room temperature. On the contrary, the anomalous Hall conductivity for $B||c$ (σ_{xy}^A) goes through a maximum at $T \approx 170$ K [see Fig. 5(a)], and reaches higher values than in the FM phase. The corresponding anomalous Nernst conductivity (ANC, α_{xy}^A/T) slowly decreases with increasing temperature [see Fig. 5(b)].

It is worth noting here that a sizeable anomalous response was already reported in other nonmagnetic topological materials [52,53]. The lack of correlation between magnetization and the ANE was even used to indicate that the observed phenomenon is due to nonzero Berry curvature [44]. In topological semimetals the AHE as well as the ANE originate from large Berry curvature generated by Weyl nodes and their presence in the paramagnetic phase of CeAlSi was recently confirmed experimentally [22]. In the presence of a finite Berry curvature, σ_{xy}^A and α_{xy}^A can be calculated as [53,54]

$$\sigma_{xy}^A = \frac{e^2}{\hbar}\sum_n \int \frac{d^3k}{(2\pi)^3}\Omega_{xy}^n f_n, \tag{8}$$

$$\alpha_{xy}^A = -\frac{1}{T}\frac{e}{\hbar}\sum_n \int \frac{d^3k}{(2\pi)^3}\Omega_{xy}^n\Big[(E_n - E_F)f_n + k_BT\ln\Big(1+\exp\frac{(E_n-E_F)}{-k_BT}\Big)\Big], \tag{9}$$

where f_n is the Fermi-Dirac distribution, E_F represents the Fermi energy, Ω_{xy}^n is the Berry curvature, and E_n are the eigenenergies for eigenstates n. From the above equations, a general form of ANC and AHC can be written as [51]

$$\lambda_{xy} = \frac{e^2}{\hbar}\sum_n \int \frac{d^3k}{(2\pi)^3}\Omega_{xy}^n w_\lambda(E_n - E_F) \text{ with } \lambda = \sigma, \alpha. \tag{10}$$

Hence, both anomalous conductivities are basically the product of Ω_{xy}^n and weighting factor (w), where the latter reads as [51]

$$w_\sigma(E_n - E_F) = f_n^T(E_n - E_F), \tag{11}$$

$$w_\alpha(E_n - E_F) = -\frac{1}{eT}\Big[(E_n - E_F)f_n^T + k_BT\ln\Big(1+\exp\frac{(E_n-E_F)}{-k_BT}\Big)\Big]. \tag{12}$$

Here f_n^T is the Fermi-Dirac distribution function at a given temperature. To model the temperature dependencies of σ_{xy}^A and α_{xy}^A in the PM phase, we introduce a single-band toy model including a nonzero Berry curvature in the vicinity of the Weyl points. $\Omega_{xy}(E)$ is simplistically assumed to change linearly at the Weyl node from positive to negative (see in Fig. S4 in the SM [26]). To match the experimental results, we restricted the energy range of nonzero Ω_{xy} to F $\pm$ 25 meV, which is similar to the range reported in Ref. [51]. As for the energy distance between the Fermi level and a Weyl node, the electronic structure calculations reported by [21] for CeAlSi indicate two sets W_1 and W_2 present close to E_F, which are expected to dominate the low energy physics of this material [21]. Each set contains different Weyl points defined as $W_1^{1,2,3,4}$ and $W_2^{1,2,3,4}$. In our model, the Weyl node is placed at -20 meV away from the E_F, which is consistent with the position of the W_2 nodes [21]. The calculated energy dependencies of AHC, ANC, and w at room temperature are shown in Fig. S4 of the SM [26]. The temperature dependencies of σ_{xy}^A and α_{xy}^A/T calculated using Eqs. (8) and (9) are presented in Fig. 5 as solid lines along with the experimental data. They appear to be governed by a broadening of the Fermi function with temperature, which allows states further away from the E_F to be included in the integration [44,52,53].

Apparently, this crude approach reproduces the characteristics of the experimental data quite well, reflecting differences between energy dependencies of weighting factors for the anomalous Hall and Nernst effects. Namely, the calculated σ_{xy}^A increases up to $T \approx 170$ K, reaches a maximum, and then decreases, while α_{xy}^A/T slowly decreases with the increasing temperature at a rate similar to the one observed in the experiment. Moreover, the signs of both σ_{xy}^A and α_{xy}^A/T also match the experimental data.

V. CONCLUSION

We studied the anomalous Hall and Nernst effects in the noncollinear Weyl semimetal CeAlSi from room to low temperature. In the ferromagnetic phase, the anomalous Hall conductivity turns out to be positive for the magnetic field applied along the magnetically hard axis ($\sigma_{xy}^A > 0$) and negative for B parallel to the easy axis ($\sigma_{yz}^A < 0$). Density functional theory calculations attributed the different signs of the AHE to a shift of Weyl points along the Γ-X direction and this shift is induced by the reconstructions in the band structure driven by the magnetic configuration. In the paramagnetic phase, σ_{yz}^A significantly decreases, whereas σ_{xy}^A reaches values even higher than at the low-temperature limit. The temperature dependence of σ_{xy}^A as well as the respective Nernst conductivity (α_{xy}^A) can be well approximated using a simple model assuming the presence of a Weyl point in the vicinity of the Fermi level. Properties of the anomalous Hall and Nernst effects appear to be dominated by **k**-space topology at both low and high temperatures.

Note added. After submission of this paper, we became aware of a very recent work that also reports on the anomalous Hall and Nernst effect in CeAlSi [55].

ACKNOWLEDGMENTS

We acknowledge W. Brzezicki, R. Citro, and K. Das for the useful discussions. This work was supported by the Foundation for Polish Science through the International Research Agendas program cofinanced by the European Union within the Smart Growth Operational Programme. A.F. was supported by the Polish National Science Centre under Project No. 2020/37/B/ST5/02299. We also acknowledge the access to the computing facilities of the Interdisciplinary Center of Modeling at the University of Warsaw, Grants No. G84-0, No. GB84-1, and No. GB84-7. We acknowledge the CINECA award under the ISCRA initiative IsC93 "RATIO" and IsC99 "SILENTS" grants for the availability of high-performance computing resources and support. The work at Boston College was funded by the National Science Foundation under Award No. DMR-2203512.

[1] N. P. Armitage, E. J. Mele, and A. Vishwanath, Weyl and Dirac semimetals in three-dimensional solids, Rev. Mod. Phys. **90**, 015001 (2018).

[2] B. Yan and C. Felser, Topological materials: Weyl semimetals, Annu. Rev. Condens. Matter Phys. **8**, 337 (2017).

[3] R. Islam, B. Ghosh, G. Cuono, A. Lau, W. Brzezicki, A. Bansil, A. Agarwal, B. Singh, T. Dietl, and C. Autieri, Topological states in superlattices of HgTe class of materials for engineering three-dimensional flat bands, Phys. Rev. Research **4**, 023114 (2022).

[4] A. S. Wadge, B. J. Kowalski, C. Autieri, P. Iwanowski, A. Hruban, N. Olszowska, M. Rosmus, J. Kołodziej, and A. Wiśniewski, Topological Lifshitz transition in Weyl semimetal NbP decorated with heavy elements, Phys. Rev. B **105**, 235304 (2022).

[5] X. Wan, A. M. Turner, A. Vishwanath, and S. Y. Savrasov, Topological semimetal and Fermi-arc surface states in the electronic structure of pyrochlore iridates, Phys. Rev. B **83**, 205101 (2011).

[6] X. Huang, L. Zhao, Y. Long, P. Wang, D. Chen, Z. Yang, H. Liang, M. Xue, H. Weng, Z. Fang, X. Dai, and G. Chen, Observation of the Chiral-Anomaly-Induced Negative Magnetoresistance: In 3D Weyl Semimetal TaAs, Phys. Rev. X **5**, 031023 (2015).

[7] J. Xiang, S. Hu, Z. Song, M. Lv, J. Zhang, L. Zhao, W. Li, Z. Chen, S. Zhang, J. T. Wang, Y. F. Yang, X. Dai, F. Steglich, G. Chen, and P. Sun, Giant Magnetic Quantum Oscillations in the Thermal Conductivity of TaAs: Indications of Chiral Zero Sound, Phys. Rev. X **9**, 031036 (2019).

[8] P. K. Tanwar, M. S. Alam, M. Ahmad, D. Kaczorowski, and M. Matusiak, Severe violation of the Wiedemann-Franz law in quantum oscillations of NbP, Phys. Rev. B **106**, L041106 (2022).

[9] I. Belopolski, K. Manna, D. S. Sanchez, G. Chang, B. Ernst, J. Yin, S. S. Zhang, T. Cochran, N. Shumiya, H. Zheng, B. Singh, G. Bian, D. Multer, M. Litskevich, X. Zhou, S. M. Huang, B. Wang, T. R. Chang, S. Y. Xu, A. Bansil *et al.*, Discovery of topological Weyl fermion lines and drumhead surface states in a room temperature magnet, Science **365**, 1278 (2019).

[10] K. Kim, J. Seo, E. Lee, K. T. Ko, B. S. Kim, B. G. Jang, J. M. Ok, J. Lee, Y. J. Jo, W. Kang, J. H. Shim, C. Kim, H. W. Yeom, B. Il Min, B. J. Yang, and J. S. Kim, Large anomalous Hall current induced by topological nodal lines in a ferromagnetic van der Waals semimetal, Nat. Mater. **17**, 794 (2018).

[11] H. B. Noam Morali, R. Batabyal, P. K. Nag, E. Liu, Q. Xu, Y. Sun, B. Yan, C. Felser, and N. Avraham, Fermi-arc diversity on surface terminations of the magnetic Weyl semimetal $Co_3Sn_2S_2$, Science **365**, 1286 (2019).

[12] E. Liu, Y. Sun, N. Kumar, L. Muechler, A. Sun, L. Jiao, S. Y. Yang, D. Liu, A. Liang, Q. Xu, J. Kroder, V. Süß, H. Borrmann, C. Shekhar, Z. Wang, C. Xi, W. Wang, W. Schnelle, S. Wirth, Y. Chen, S. T. B. Goennenwein, and C. Felser, Giant anomalous Hall effect in a ferromagnetic kagome-lattice semimetal, Nat. Phys. **14**, 1125 (2018).

[13] Y. Yao, L. Kleinman, A. H. MacDonald, J. Sinova, T. Jungwirth, D. sheng Wang, E. Wang, and Q. Niu, First Principles Calculation of Anomalous Hall Conductivity in Ferromagnetic bcc Fe, Phys. Rev. Lett. **92**, 037204 (2004).

[14] J. Gaudet, H. Y. Yang, S. Baidya, B. Lu, G. Xu, Y. Zhao, J. A. Rodriguez-Rivera, C. M. Hoffmann, D. E. Graf, D. H. Torchinsky, P. Nikolić, D. Vanderbilt, F. Tafti, and

C. L. Broholm, Weyl-mediated helical magnetism in NdAlSi, Nat. Mater. **20**, 1650 (2021).

[15] R. Yang and M. Corasaniti, Charge dynamics of a noncentrosymmetric magnetic Weyl semimetal, npj Quantum Mater. **7**, 101 (2022).

[16] P. Li, J. Koo, W. Ning, J. Li, L. Miao, L. Min, Y. Zhu, Y. Wang, N. Alem, C. X. Liu, Z. Mao, and B. Yan, Giant room temperature anomalous Hall effect and tunable topology in a ferromagnetic topological semimetal Co_2MnAl, Nat. Commun. **11**, 3476 (2020).

[17] K. Geishendorf, P. Vir, C. Shekhar, C. Felser, J. I. Facio, J. Van Den Brink, K. Nielsch, A. Thomas, and S. T. B. Goennenwein, Signatures of the magnetic entropy in the thermopower signals in nanoribbons of the magnetic Weyl semimetal $Co_3Sn_2S_2$, Nano Lett. **20**, 300 (2020).

[18] S. Itoh, Y. Endoh, T. Yokoo, S. Ibuka, J. G. Park, Y. Kaneko, K. S. Takahashi, Y. Tokura, and N. Nagaosa, Weyl fermions and spin dynamics of metallic ferromagnet $SrRuO_3$, Nat. Commun. **7**, 11788 (2016).

[19] D. J. Groenendijk, C. Autieri, T. C. Van Thiel, W. Brzezicki, J. R. Hortensius, D. Afanasiev, N. Gauquelin, P. Barone, K. H. W. Van Den Bos, S. Van Aert, J. Verbeeck, A. Filippetti, S. Picozzi, M. Cuoco, and A. D. Caviglia, Berry phase engineering at oxide interfaces, Phys. Rev. Res. **2**, 023404 (2020).

[20] T. C. Van Thiel, W. Brzezicki, C. Autieri, J. R. Hortensius, D. Afanasiev, N. Gauquelin, D. Jannis, N. Janssen, D. J. Groenendijk, J. Fatermans, S. Van Aert, J. Verbeeck, M. Cuoco, and A. D. Caviglia, Coupling Charge and Topological Reconstructions at Polar Oxide Interfaces, Phys. Rev. Lett. **127**, 127202 (2021).

[21] H. Y. Yang, B. Singh, J. Gaudet, B. Lu, C. Y. Huang, W. C. Chiu, S. M. Huang, B. Wang, F. Bahrami, B. Xu, J. Franklin, I. Sochnikov, D. E. Graf, G. Xu, Y. Zhao, C. M. Hoffman, H. Lin, D. H. Torchinsky, C. L. Broholm, A. Bansil, and F. Tafti, Noncollinear ferromagnetic Weyl semimetal with anisotropic anomalous Hall effect, Phys. Rev. B **103**, 115143 (2021).

[22] A. P. Sakhya, C. Huang, G. Dhakal, X. Gao, S. Regmi, X. Yao, R. Smith, M. Sprague, and B. Singh, Observation of Fermi arcs and Weyl nodes in a non-centrosymmetric magnetic Weyl semimetal, arXiv:2203.05440.

[23] M. M. Piva, J. C. Souza, V. Brousseau-Couture, K. R. Pakuszewski, J. K. John, C. Adriano, M. Côté, P. G. Pagliuso, and M. Nicklas, Tuning the nontrivial topological properties of the Weyl semimetal CeAlSi, arXiv:2111.05742.

[24] C. M. Hurd, *The Hall Effect in Metals and Alloys*, International Cryogenics Monograph Series (Springer, Berlin, 1972).

[25] M. S. Alam, P. K. Tanwar, K. Dybko, A. S. Wadge, P. Iwanowski, A. Wiśniewski, and M. Matusiak, Temperature-driven spin-zero effect in $TaAs_2$, J. Phys. Chem. Solids **170**, 110939 (2022).

[26] See Supplemental Material at http://link.aps.org/supplemental/10.1103/PhysRevB.107.085102 for additional experimental data, modeled anomalous Hall and Nernst conductivities in the presence of nonzero Berry curvature, and a detailed discussion of band structure calculations.

[27] G. Kresse and J. Hafner, *Ab initio* molecular dynamics for liquid metals, Phys. Rev. B **47**, 558 (1993).

[28] G. Kresse and J. Furthmüller, Efficient iterative schemes for ab initio total-energy calculations using a plane-wave basis set, Phys. Rev. B **54**, 11169 (1996).

[29] W. E. Pickett, Implementation of the LDA + U method using the full-potential linearized augmented plane-wave basis, Phys. Rev. B **60**, 10763 (1999).

[30] A. A. Mostofi, J. R. Yates, G. Pizzi, Y. S. Lee, I. Souza, D. Vanderbilt, and N. Marzari, An updated version of WANNIER90: A tool for obtaining maximally-localised wannier functions, Comput. Phys. Commun. **185**, 2309 (2014).

[31] M. Zeer, D. Go, J. P. Carbone, T. G. Saunderson, M. Redies, M. Kläui, J. Ghabboun, W. Wulfhekel, S. Blügel, and Y. Mokrousov, Spin and orbital transport in rare-earth dichalcogenides: The case of EuS_2, Phys. Rev. Mater. **6**, 074004 (2022).

[32] W. Cao, Y. Su, Q. Wang, C. Pei, L. Gao, Y. Zhao, C. Li, N. Yu, J. Wang, Z. Liu, Y. Chen, G. Li, J. Li, and Y. Qi, Quantum oscillations in noncentrosymmetric Weyl semimetal SmAlSi, Chin. Phys. Lett. **39**, 047501 (2022).

[33] N. Nagaosa, J. Sinova, S. Onoda, A. H. MacDonald, and N. P. Ong, Anomalous Hall effect, Rev. Mod. Phys. **82**, 1539 (2010).

[34] K. S. Takahashi, H. Ishizuka, T. Murata, Q. Y. Wang, Y. Tokura, N. Nagaosa, and M. Kawasaki, Anomalous Hall effect derived from multiple Weyl nodes in high-mobility $EuTiO_3$ films, Sci. Adv. **4**, eaar7880 (2018).

[35] M. Tanaka, Y. Fujishiro, M. Mogi, Y. Kaneko, T. Yokosawa, N. Kanazawa, S. Minami, T. Koretsune, R. Arita, S. Tarucha, M. Yamamoto, and Y. Tokura, Topological kagome magnet $Co_3Sn_2S_2$ thin flakes with high electron mobility and large anomalous Hall effect, Nano Lett. **20**, 7476 (2020).

[36] B. Meng, H. Wu, Y. Qiu, C. Wang, Y. Liu, Z. Xia, S. Yuan, H. Chang, and Z. Tian, Large anomalous Hall effect in ferromagnetic Weyl semimetal candidate PrAlGe, APL Mater. **7**, 051110 (2019).

[37] J. F. Wang, Q. X. Dong, Z. P. Guo, M. Lv, Y. F. Huang, J. Sen Xiang, Z. A. Ren, Z. J. Wang, P. J. Sun, G. Li, and G. F. Chen, NdAlSi: A magnetic Weyl semimetal candidate with rich magnetic phases and atypical transport properties, Phys. Rev. B **105**, 144435 (2022).

[38] S. Onoda, N. Sugimoto, and N. Nagaosa, Intrinsic versus Extrinsic Anomalous Hall Effect in Ferromagnets, Phys. Rev. Lett. **97**, 126602 (2006).

[39] L. Berger, Side-jump mechanism for the Hall effect of ferromagnets, Phys. Rev. B **2**, 4559 (1970).

[40] A. A. Burkov, Anomalous Hall Effect in Weyl Metals, Phys. Rev. Lett. **113**, 187202 (2014).

[41] A. Sekine, D. Culcer, and A. H. MacDonald, Quantum kinetic theory of the chiral anomaly, Phys. Rev. B **96**, 235134 (2017).

[42] G. Chang, B. Singh, S. Y. Xu, G. Bian, S. M. Huang, C. H. Hsu, I. Belopolski, N. Alidoust, D. S. Sanchez, H. Zheng, H. Lu, X. Zhang, Y. Bian, T. R. Chang, H. T. Jeng, A. Bansil, H. Hsu, S. Jia, T. Neupert, H. Lin, and M. Z. Hasan, Magnetic and noncentrosymmetric Weyl fermion semimetals in the RAlGe family of compounds (R = Rare Earth), Phys. Rev. B **97**, 041104(R) (2018).

[43] T. Liang, Q. Gibson, J. Xiong, M. Hirschberger, S. P. Koduvayur, R. J. Cava, and N. P. Ong, Evidence for massive bulk Dirac fermions in $Pb_{1-x}Sn_xSe$ from Nernst and thermopower experiments, Nat. Commun. **4**, 2696 (2013).

[44] T. Liang, J. Lin, Q. Gibson, T. Gao, M. Hirschberger, M. Liu, R. J. Cava, and N. P. Ong, Anomalous Nernst Effect in the Dirac Semimetal Cd_3As_2, Phys. Rev. Lett. **118**, 136601 (2017).

[45] J. Hu, B. Ernst, S. Tu, M. KuveŽdić, A. Hamzić, E. Tafra, M. Basletić, Y. Zhang, A. Markou, C. Felser, A. Fert, W. Zhao,

J. P. Ansermet, and H. Yu, Anomalous Hall and Nernst Effects in Co_2TiSn and $Co_2Ti_{0.6}V_{0.4}Sn$ Heusler Thin Films, Phys. Rev. Appl. **10**, 044037 (2018).

[46] Y. Pu, D. Chiba, F. Matsukura, H. Ohno, and J. Shi, Mott Relation for Anomalous Hall and Nernst Effects in $Ga_{1-x}Mn_xAs$ Ferromagnetic Semiconductors, Phys. Rev. Lett. **101**, 117208 (2008).

[47] D. Xiao, Y. Yao, Z. Fang, and Q. Niu, Berry-Phase Effect in Anomalous Thermoelectric Transport, Phys. Rev. Lett. **97**, 026603 (2006).

[48] A. K. Nayak, J. E. Fischer, Y. Sun, B. Yan, J. Karel, A. C. Komarek, C. Shekhar, N. Kumar, W. Schnelle, J. Kübler, C. Felser, and S. S. P. Parkin, Large anomalous Hall effect driven by a nonvanishing berry curvature in the noncolinear antiferromagnet Mn_3Ge, Sci. Adv. **2**, e1501870 (2016).

[49] R. Di Capua, M. Verma, M. Radovic, V. N. Strocov, C. Piamonteze, E. B. Guedes, N. C. Plumb, Y. Chen, M. D'Antuono, G. M. De Luca, E. Di Gennaro, D. Stornaiuolo, D. Preziosi, B. Jouault, F. Miletto Granozio, A. Sambri, R. Pentcheva, G. Ghiringhelli, and M. Salluzzo, Orbital selective switching of ferromagnetism in an oxide quasi two-dimensional electron gas, npj Quantum Mater. **7**, 41 (2022).

[50] M. Yao, H. Lee, N. Xu, Y. Wang, J. Ma, O. V. Yazyev, Y. Xiong, M. Shi, G. Aeppli, and Y. Soh, Switchable Weyl nodes in topological kagome ferromagnet Fe_3Sn_2, arXiv:1810.01514.

[51] J. Noky, J. Gooth, C. Felser, and Y. Sun, Characterization of topological band structures away from the Fermi level by the anomalous Nernst effect, Phys. Rev. B **98**, 241106(R) (2018).

[52] T. Liang, J. Lin, Q. Gibson, S. Kushwaha, M. Liu, W. Wang, H. Xiong, J. A. Sobota, M. Hashimoto, P. S. Kirchmann, Z. X. Shen, R. J. Cava, and N. P. Ong, Anomalous Hall effect in $ZrTe_5$, Nat. Phys. **14**, 451 (2018).

[53] F. Caglieris, C. Wuttke, S. Sykora, V. Süss, C. Shekhar, C. Felser, B. Büchner, and C. Hess, Anomalous Nernst effect and field-induced Lifshitz transition in the Weyl semimetals TaP and TaAs, Phys. Rev. B **98**, 201107(R) (2018).

[54] D. Xiao, M. C. Chang, and Q. Niu, Berry phase effects on electronic properties, Rev. Mod. Phys. **82**, 1959 (2010).

[55] E. Cheng, L. Yan, X. Shi, M. Behnami, J. Yuan, Y. Xu, Y. Xu, Y. Wan, W. Xia, N. Pavlovskii, D. C. Peets, W. Zhao, Y. Guo, S. Li, W. Yang, and B. Büchner, Anomalous transverse transport and phase transitions in Weyl semimetals RAlSi (R = La, Ce), arXiv:2301.03800.

Correction: The units shown on the y axis of the previously published Figure 5(b) were incorrect. The figure has been replaced.